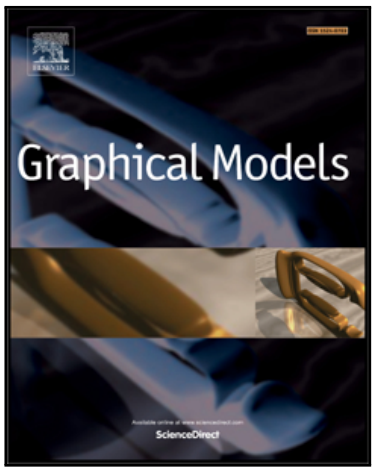

Pore-scale Flow Simulation in Anisotropic Porous Material via Fluid-structure Coupling

Chen Li, Changbo Wang, Shenfan Zhang, Sheng Qiu, Hong Qin

PII: S1524-0703(17)30064-4
DOI: 10.1016/j.gmod.2017.12.001
Reference: YGMOD 988

To appear in: *Graphical Models*

Received date: 2 March 2017
Revised date: 19 December 2017
Accepted date: 22 December 2017

Please cite this article as: Chen Li, Changbo Wang, Shenfan Zhang, Sheng Qiu, Hong Qin, Pore-scale Flow Simulation in Anisotropic Porous Material via Fluid-structure Coupling, *Graphical Models* (2017), doi: 10.1016/j.gmod.2017.12.001

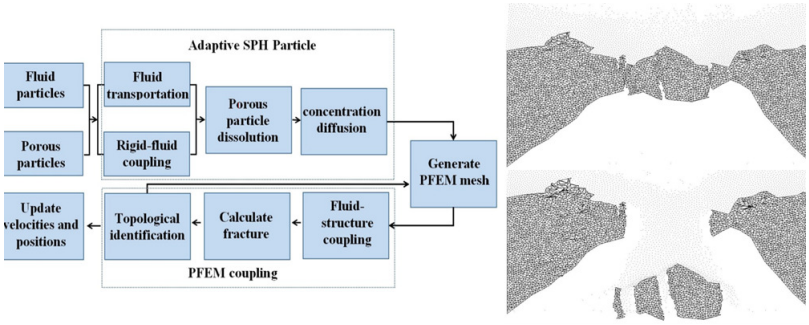

Pore-scale Flow Simulation in Anisotropic Porous Material via Fluid-structure Coupling

Chen Li[a], Changbo Wang[*,a], Shenfan Zhang[a], Sheng Qiu[a], Hong Qin[b]

[a]*School of Computer Science and Software Engineering, East China Normal University, Shanghai, China*
[b]*Department of Computer Science, Stony Brook University, Stony Brook, USA*

Abstract

This paper describes a novel hybrid method for fluid simulation of saturating anisotropic porous material via fluid-structure coupling. Our framework employs particle finite element method (PFEM) that not only adopts Lagrangian scheme to model the motion of freely-moving particles, but also produces the extended Delaunay Tessellation to furnish the governing equations with FEM discretization. We first employ adaptive smoothed particle hydrodynamics (SPH) to simulate porous flow respecting the anisotropic permeability with little cost. Second, the extended Delaunay Tessellation is obtained to solve differential equations for skeletal deformation. Third, a hybrid particle system is adopted to track the surface and topological changes. At the physical level, we introduce dynamic permeability considering skeletal deformation via fluid-structure coupling. At the geometric level, PFEM reduces the computational cost and effectively tracks topological changes. Moreover, our implementation on CUDA improves the performance in high-quality physics-based graphics applications. Consequently, the proposed method realistically reproduces interactions between pore-scale flow and anisotropic porous material.

Keywords: Anisotropic porous material, Particle finite element method, Fluid-structure coupling, Realistic simulation

1. Introduction and Motivation

Geologic substance, such as soil, grotto, or karst, are porous when examined at the appropriate scale [1], which exhibits a large range of interesting phenomena, including dissolution, merging, or fracture, etc. Physically-correct animation of porous media still remains a difficult problem in computer graphics. In most fluid-rigid and fluid-deformable animations, the prior focus has been mostly on the impenetrable solid objects and/or non-porous deformable objects [2]. Recently great progress has been made in absorption and diffusion of pore fluid through their bodies [3, 4], but earlier works usually ignore the anisotropy factor of geologic form and substance. Geologic materials exhibit certain degree of anisotropy due to stratification associated with forming processes such as sedimentation, illuviation, compaction, and particle orientation [5]. Anisotropic permeability and porosity [6] are typically characterized by directional hydraulic conductivity in tensorial representation, which is the so-called conceptual "layered-cake" model. The rapid, precise, and visually realistic simulation of the aforementioned materials for graphics applications, while respecting the complicated form and structure variation and fluid-solid interaction, remains technically challenging due to the complicated multi-interaction among many substances and substrate. This paper seeks a feasible solution towards the above technical difficulties.

One possible way is to rely on complex meshing and its time-varying structure, however, anisotropic mesh generation and analysis are time-consuming in principle. For example, the adaptive remeshing technique used in cloth simulation [7] has limitations when dealing with incompressible materials. Even worse, classical seepage mechanics commonly assumes the porous media is fully rigid, that means the solid skeleton won't produce any elastic or plastic deformation while pressure of seepage changes, thus such problem is simplified as non-coupling problem. But such strong assumption has various drawbacks, most natural geologic substance and artificial porous solids are deformable objects. The pore pressure change will cause not only the change of strain which will give rise to different permeability and porosity, but also influence the motion and pressure distribution of seepage conversely [8]. So the strong coupling of the effective strain of porous media and seepage is inevitable in simulation of seepage in porous media.

In this work, we deviate from the conventional meshing idea and propose a novel particle-based approach to simulate pore-scale flow in porous media. Our framework for fluid absorption and diffusion intends to unify the prior work of [9, 10] and we extend it to simulate the dissolution of soils and the diffusion of muddy water according to [11]. Considering the structure of anisotropic materials, adaptive smoothed particle hydrodynamics (SPH) [12] is applied to analyze the stain field in order to capture seepage along different directions with minimum computational cost. Meanwhile, considering deformation and possible destruction of the skeleton caused by effective stress in porous media in fluid-structure coupling, we propose a dynamic seepage coupling model. Then, particle finite element method (FEM) [13] is introduced to solve the above model, where all the geometrical and mechanical information is attributed to SPH particles. Meshless FEM [14] is then used to compute the forces acting on each individual particle and geometric boundaries of the domain are defined via the powerful Alpha-shape method [15]. In this way, the solver has the advantages of a flexible meshless method, while also preserv-

ing the classical advantages of FEM. To obtain richer pore flow and solid deformation details, we adopt the adaptive weighted Alpha shape [15] and develop rendering techniques to support several wet-saturation levels. The main contributions of this paper can be summarized as follows:

- **An efficient physical model considering dynamic anisotropic permeability and fluid-structure coupling in porous media.** Our method employs equivalent continuum model to represent the porous media, and adopts dynamic porosity and permeability pertinent to anisotropy and skeleton deformation. Moreover, considering the skeletal deformation of porous media and the compressibility of fluid, we employ the principle of effective stress in the dynamic fluid-structure coupling model to capture the porous skeletal deformation and fracture physically.

- **A new particle FEM-based framework coupled with adaptive SPH for the tight coupling of complex various materials.** Based on the idea from novel particle FEM, we introduce a unified meshless solver for tight coupling between pore-scale flow and anisotropic porous material, which can emancipate complex mesh operation with SPH particles and enjoy the simplicity of the shape functions in finite element method (FEM). Our method adopts the macroscopic scale porous material representation in [9], and with that we can simplify anisotropy of geologic materials based on adaptive SPH approximation of pore pressure field to track fluid absorption and diffusion. Then extended Delaunay Tessellation (EDT) is established with SPH particles for calculating skeletal deformation and fracture of porous media. Also phase transition will occur at fully-saturated high-porosity particles to track muddy water during the permeation, and LLSPH [11] is adopted to simulate the mixture of muddy water and original water.

- **Graphics-friendly unified particle framework for surface reconstrction with CUDA acceleration.** The unified particle centric framework is established to transform physical properties between flexible SPH particles and EDT based on particle FEM. Towards better visual realism, our new framework employs adaptive weighted Alpha shape based topological analysis and link-based surface tracing to reconstruct saturation-sensitive porous media surface, while fluid surface is reconstructed based on the marching cubes (MC) method [16]. The unified framework also offers advantage in parallel acceleration with CUDA to guarantee satisfactory performance for graphics applications.

The rest of the paper is organized as follows. After briefly documenting previous works in Section 2, we describe the dynamic model of pore flow in porous media, while considering fluid-structure coupling effects in Section 3. Then the framework based on particle FEM and adaptive SPH is introduced in Section 4. Section 5 explains how we deal with shape geometry as well as parallel implementation in our experiments. Section 6 discusses the experimental results and limitations, and we draw the conclusion in Section 7.

2. Related Work

2.1. Hybrid Method in Fluid Simulation

A large amount of work on both pure Eulerian and pure Lagrangian methods have been proposed, where SPH [17, 18] may be the most popular Lagrangian method. Though SPH is fast and suitable for graphics applications, it has a hard time dealing with mechanics problems pertinent to solid structure. On the other hand, traditional FEM is powerful but time consuming due to complex remeshing operation.

Recently, the idea of hybrid representation is gaining popularity in fluid simulation, several works couples the Lagrangian particles with gird-based methodology [19], such as SPH coupled with Euler mesh [20], particle level set [21]. Sin et al. [22] computed a Voronoi diagram with the sample points to solve pressure projection. Thürey et al. [23] merged Euler surface tension and FEM based wave details. Pfaff et al. [24] employed triangle mesh as a high-resolution surface representation combined with a coarse Eulerian solver. Wang et al. [25] preserved surface details such as spray and foam via coupling band between particles and fluid grids occuring in the vicinity. Chentanez et al. [26] proposed a framework coupling Eulerian grid, particles, and height field for large-scale liquid phenomena. Müller et al. [27] developed an SPH approach that augments particles with a sample of angular momentum.

The first combination of Lagrangian and FEM methods can be found in MFEM [28], where the extended Delaunay tessellation is used in mesh reconstruction, then Idelsohn et al. evolved the PFEM method, combining a particle method together with the MFEM and the Alpha-shape method. The key feature of the method is the use of Lagrangian description to model the motion of nodes in the structure domain. The difference between the PFEM and hybrid methods such as PIC [29] is that, the information in the PFEM is nodal-based, the element mesh is used to obtain the values of the state variables at the nodes. Inspired by interesting ideas resulted from the above methods, we adopt a hybrid particle-based method supporting SPH-based fluid-rigid two-way coupling in order to reconstruct free surface and PFEM based fluid-structure coupling in order to track fracture in porous media. Consequently, time-consuming data transfer and remeshing are avoided, benefiting from nodal-based representation.

2.2. Pore Flow Simulation

Our work is closely related to simulation of fluid flow through porous materials and meshless methods in computer graphics. To simulate pore flow, researchers have proposed varieties of approaches. Chu and Tai[30] presented a GPU-based method for simulating ink dispersion in absorbent paper based on the Lattice Boltzmann equation. Kramer et al. [31] proposed an algorithm based on a combination of single domain and subdomain boundary element method (BEM) to model fluid flow in porous media, coupled with the energy equation using the

Boussinesq approximation. Um et al. [3] used a two-layer model to handle porous shells that interact with water integrated with the position based dynamics(PBD) for object simulation.

On the other hand, various works have been proposed for modeling of capillary pores and SPH simulations of flow. Sawley et al. [32] simulated flow in porous media and resin transfer based on a mesoscopic scale modeling using SPH. Lenaerts et al. [9] introduced Darcy's Law into SPH to simulate porous flow at a macroscopic scale, and reused the particle representation of deformable objects. Lin [10] proposed similar method in coupling hair and SPH fluids and made an extension by adopting anisotropic permeability in the diffusion process to model the directional fluid flow along void space within the hair volume. Huber et al. [4] introduced a hybrid model for wetting effects on a flat surface including water absorption and diffusion, and they modeled the flow using SPH and the cloth using mesh.

Considering the anisotropy, adaptive SPH [33, 34] is adopted with anisotropic kernel instead of isotropic kernel to reflect different physical properties in directions. Liu et al. [35] used adaptive SPH to improve the stability when simulating deformable solids using fixed anisotropic axes. In our work, we adopt the method of [9, 36] and adaptive SPH with free axes as particle solver, because it is stable and economical to deal with the relation between anisotropy and saturation.

2.3. Coupling of Pore Flow and Porous Media

Research on fluid sorption in porous media has been performed for over a century ago in geology and computational physics, dating back to [37, 38]. The latest models are capable of describing more complex coupling effects, such as deformable porous media [39], multiphase flow [40, 41], wettability influences [42] and particle containing flows [43].

Luo et al. [44] established a fully-coupling three-dimensional mathematical model of seepage and stress considering the nonlinear characteristics and the dynamic variation of hydraulic conductivity of soils with stress. Lichtner and Kang [45] considered kinetics, porosity evolution caused by volume changes during reaction, advective, and diffusive transport, whereas they didn't consider the mechanics of rock deformation. Keller et al. [46] coupled a visco-elasto-plastic rheology for both shear and compaction deformation of the host rock. Malvoisin et al. [47] were tracking the changes in density, porosity, permeability, and fluid pressure during fluid flow in porous media which influence fluid flow and rock deformation.

However in computer graphics various frameworks for interaction between deformable objects or rigid and fluids have been proposed [48, 49] or pore flow through porous media [9], but little work focuses on coupling of dynamic pore flow and deformable porous media, so we try to introduce the fully-coupled model into graphics with simplified discrete calculation.

3. Dynamic Modeling of Pore Flow in Porous Media towards Fluid-structure Coupling

Our physical model is mainly motivated by geo-mechanics. Similar to [9], we adopt the equivalent continuum model to represent porous media and deal with pore flow. Then dynamic porosity and permeability pertinent to anisotropy and skeletal deformation of porous media is considered together with stress-strain constitutive equation in fluid-structure coupling in order to achieve a fully coupled physical model. Table 1 documents the parameters used in this and the following sections.

Table 1: Key parameters and constants and their descriptions.

Parameters	Description	Constants	Description
$\mathbf{x}_i$	position	η	viscosity
m_i	mass	k^c	potential coefficient
V_i	volume	k^p	pressure coefficient
ρ_i	density	α	potential coefficient
ϕ_i	porosity	γ	pressure coefficient
$\mathbf{K}_i$	permeability	ρ_0	rest density
m_{pi}	absorbed mass	β	diffusion coefficient
S_i	saturation	K_s	solid modulus
P_i^p	pore pressure	K_f	fluid modulus
P_i^c	capillary potential	λ	Lamé constant
$\mathbf{G}$	anisotropic tensor	μ	Lamé constant
$\mathbf{v}_{pi}$	pore velocity	B	Biot coefficient
ε_v	volumetric strain	ϕ_0	initial porosity
$\mathbf{u}(W_x, W_y, W_z)$	displacement	β_s	temperature coefficient
σ	stress	E	Young's modulus
U	strain energy	ν	poisson ratio
$\mathbf{p}_r$	linear momentum	$\mathbf{L}_r$	angular momentum

3.1. Pore Flow in Equivalent Continuum Model

Porous media often exhibit a variety of heterogeneities, such as fractures, fissures, and macropores or intra-aggregate pores. Water flows unevenly through an intricate network of paths formed by fracture intersections, as a result, the discontinuous nature of the permeability and porosity gives rise to challenge in modeling. As an alternative, it can be avoided by simplifying them by averaged values in the equivalent continuum model.

In the equivalent continuum approach, pore-fractures are not modeled explicitly, instead the bedrock is treated as a continuum with properties derived from an averaging procedure. The hydraulic properties of the domain are averaged over the sub-volume, or representative elementary volume, containing sufficiently large number of pore-fractures. Pore flow is assumed to allow passing through the whole system.

Each porous elementary volume p is located at position $\mathbf{x}$, with mass m, volume V, density ρ, porosity ϕ, permeability $\mathbf{K}$, and ϕ denotes the volume fraction of the interconnected void space that can absorb fluid, so p can hold absorbed fluid mass $m_p \leq \rho^{fluid}\phi V$, and the saturation S:

$$S = \frac{m_p}{\rho^{fluid}\phi V}. \tag{1}$$

What we cannot ignore is that geologic materials usually have certain degree of anisotropy due to stratification in forming processes such as sedimentation, illuviation, and compaction. Unlike isotropic permeability, anisotropic permeability $\mathbf{K}$ requires tensorial representation, the accentuated directionality represents a challenge to characterization and prediction of pore process. Therefore, a second-order symmetric tensor is used to

represent the permeability $\mathbf{K}$ along different directions and updated with $\mathbf{K} = \frac{K}{K_0}\mathbf{R}^T\mathbf{K}_0\mathbf{R}$, where $\mathbf{R}$ is the rotation matrix of rigid body it belongs to. Then Darcy's Law[37] is introduced by [9, 36] to govern the pore velocity $\mathbf{v}_p$:

$$\mathbf{v}_p = -\frac{\mathbf{K}}{\phi\eta}(\nabla P^p - \nabla P^c - \rho\mathbf{g}), \tag{2}$$

where $\eta = 0.1$ is the viscosity in our expirment, P^p and P^c are the pore pressure and capillary potential:

$$P^c = k^c(1-S)^\alpha, P^p = k^p S\left(\left(\frac{\rho}{\rho_0}\right)^\gamma - 1\right). \tag{3}$$

Here constants k^c and $0 < \alpha < 1$ control the strength of the potential, k^p and $\gamma = 7$ control the pore pressure and ρ_0 is the fluid rest density, for more technical details please refer to [50, 51].

Once the pore velocity field is obtained, the evolution of the absorbed fluid mass m_p is described as diffusion in an Eulerian manner [10]:

$$\rho\frac{\partial m_p}{\partial t} = d\nabla^2 m_p, \tag{4}$$

where d is the diffusion coefficient [9]. We ignore the emission due to the fact that the geologic materials tend to be open-air drying by transporting fluid to air slowly.

3.2. Dynamic Fluid-structure Coupling Effects

As we described above, classical percolation theory usually assumes that the porous media is fully rigid, that means the skeleton of porous media doesn't have any elastic or plastic deformation during the pore pressure field change, thus the fluid-structure coupling is ignored in the previous methods. But, irrespective of the fact that natural geologic materials or artificial porous materials are mostly deformable, on one hand, the change of the pore pressure field will cause the variety of effective stress in porous media skeleton, which further influences dynamic porosity and permeability; on the other hand, the skeleton conversely influences the motion and pressure of pore flow [8, 52].

Assume that the skeleton volume of porous media is V_s, and the bulk volume is V_b, so pore volume $V_p = V_b - V_s$, ΔV denotes the corresponding volume change, $\mathbf{u}(W_x, W_y, W_z)$ is the skeletal displacement in 3d, then the volumetric strain ε_v is

$$\varepsilon_v = \nabla\cdot\mathbf{u} = \frac{\partial W_x}{\partial x} + \frac{\partial W_y}{\partial y} + \frac{\partial W_z}{\partial z}. \tag{5}$$

According to the definition of porosity:

$$\phi = 1 - \frac{V_{s0}(1+\Delta V_s/\Delta V_{s0})}{V_{b0}(1+\Delta V_b/\Delta V_{b0})} = 1 - \frac{1-\phi_0}{1+\varepsilon_v}(1+\frac{\Delta V_s}{\Delta V_{s0}}), \tag{6}$$

if we treat the skeleton volume change as elastic deformation:

$$\frac{\Delta V_s}{\Delta V_{s0}} = -\frac{\Delta p}{K_s} + \beta_s\Delta T, \tag{7}$$

where the former term reflects volume change caused by pore pressure, and the latter term is the temperature effect, ΔT is the difference of temperature and β_s is a constant, in our experiments, we assume the ground is constant-temperature, so the latter item is neglected by setting $\beta_s = 0$. Then we have the expression:

$$\phi = 1 - \frac{(1-\phi_0)(1-\Delta p/K_s)}{1+\varepsilon_v}, \tag{8}$$

where K_s is the bulk elastic compression modulus of porous media. If the porous media is fully rigid ($\varepsilon_v = 0$) or fluid($\phi_0 = 1$), then $\phi = \phi_0$. Similarly, the absolute value of permeability k is not a constant either:

$$k = \frac{k_0}{1+\varepsilon_v}[1 + \frac{\varepsilon_v - \Delta p/K_s(1-\phi_0)}{\phi_0}]^3. \tag{9}$$

Due to the nature of pore flow via porous media, both the fluid and skeleton have certain velocity, so the velocity of fluid $\mathbf{v}_f$ is

$$\mathbf{v}_f = \mathbf{v}_r + \mathbf{v}_s, \tag{10}$$

where $\mathbf{v}_s = \partial W/\partial t$ is the absolute speed of skeleton, $\mathbf{v}_r$ is the relative speed of fluid to skeleton, combining the continuity equations of skeleton and pore flow, Eq. 10 can be handled as:

$$\phi\nabla\cdot\mathbf{v}_r + \nabla\cdot\mathbf{v}_s + \frac{1-\phi}{\rho_s}\frac{\partial\rho_s}{\partial t} + \frac{\phi}{\rho_f}\frac{\partial\rho_f}{\partial t} = 0. \tag{11}$$

Then substitute Darcy's Law and the state equation into Eq. 11:

$$-\nabla\cdot(\frac{\mathbf{K}}{\phi\eta}(\nabla P^p - \nabla P^c - \rho\mathbf{g})) + \frac{\partial\varepsilon_v}{\partial t} + \left(\frac{1-\phi}{K_s} + \frac{\phi}{K_f}\right)\frac{\partial p}{\partial t} = 0, \tag{12}$$

where K_f is the bulk elastic compression modulus of fluid.

Based on the stress-strain constitutive equation of porous media:

$$\sigma'_{ij} = \lambda\varepsilon_v\delta_{ij} + 2\mu\varepsilon_{ij}, \tag{13}$$

where $\lambda = \frac{\nu E}{(1+\nu)(1-2\nu)}$ and $\mu = \frac{E}{2(1+\nu)}$ are the Lamé constants, E is Young's modulus and ν is poisson ratio of the porous media, ε_{ij} is the pressure elements, together with the equilibrium equations of stress:

$$\sigma'_{ij} + \phi p\delta_{ij} + F_i = 0, \tag{14}$$

we have the stress field equation with $\phi, p, W_k(k = x, y, z)$:

$$\frac{\mu}{1-2\nu}\frac{\partial\varepsilon_v}{\partial k} + \mu\nabla^2 W_k + \phi\frac{\partial p}{\partial k} = 0. \tag{15}$$

After the displacement field is obtained, a stress-based fracture scheme is established to track severe fracture. We use Rankine hypothesis [53] as fracture criteria. It is stated that, if the principal stress of a point exceeds a criterion threshold of the material, a fracture is initiated and the normal of fracture surface equals to the principal stress direction. The Cauchy stress tensor σ^p is [54] is calculated with the displacement field of the porous media $\mathbf{u}(W_x, W_y, W_z)$:

$$\sigma^p(\mathbf{u}, p) = \sigma(\mathbf{u}) - Bp\mathbf{I}, \tag{16}$$

where $\mathbf{I}$ is the identity tensor and σ is the effective linear elastic stress tensor, B denotes the dimensionless Biot coefficient:

$$\sigma(\mathbf{u}) = \lambda(\nabla \cdot \mathbf{u})\mathbf{I} + 2\mu\varepsilon(\mathbf{u}). \tag{17}$$

Here the strain tensor is $\varepsilon(\mathbf{u}) = (\nabla\mathbf{u} + \nabla\mathbf{u}^T)/2$. Then the strain energy is determined with

$$U = \frac{1}{2}V(\sigma^p(\mathbf{u}, p) \cdot \varepsilon(\mathbf{u})). \tag{18}$$

For the purposes of calculating crack length, the energy release rate is defined as $G = -\partial U/\partial A$, where A is the crack area.

4. Coupling Simulation based on Particle FEM with Adaptive SPH

As described above, the model of porous media-fluid coupling will suffer from complex and time-consuming computation on anisotropic mesh, while pure particle based method can hardly deal with skeletal deformation and fracture. Here we introduce the novel particle finite element method (PFEM), a new generation of the particle method, which combines flexible adaptive SPH with anisotropic kernel and powerful FEM for fluid-structure interaction problems.

4.1. Method Overview

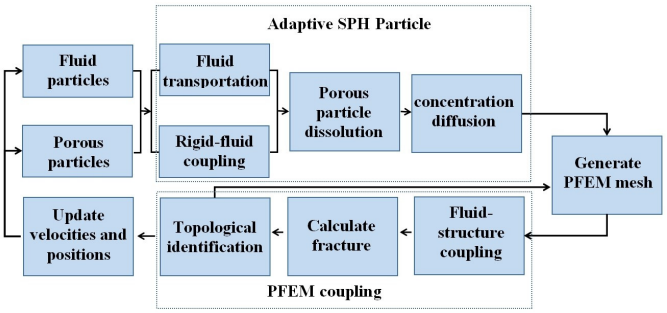

Figure 1: The core process for our unified particle framework. SPH particles hold the fluid transportation and two-way coupling as well as dissolution and diffusion in porous media, once the new PFEM mesh is established, structure and fracture is solved to deal with the topological change, finally the new particle position is calculated and go back to next time step.

Our algorithmic flow is summarized in Fig. 1. In each simulation cycle, it updates the new position and velocity based on the results of last simulation cycle, and then employs shape surface model and Marching Cubes to track the surface. We detail our operations in Algorithm 1. First, we propose momentum-conserving rigid-fluid two-way coupling based on hydro-dynamic forces [2] with PCISPH, meanwhile fluid absorption and transportation between fluid particles and porous particles are calculated with adaptive SPH. Next, we dissolve saturated particles into muddy fluid particles and calculate diffusion in fluid particles with LLSPH [11]. Then new PFEM mesh is regenerated if dissolution happens, where we can compute the dynamic porosity, permeability, pore pressure and displacement field of porous media to produce collapse at high pore pressure region. Topological identification based on our surface modeling is carried after moving mesh nodes, if severe shape change happens or the mesh has not been updated for steps, regenerate new PFEM mesh. Finally, update velocities and positions of particles for next simulation cycle driven by the updated coupling results.

4.2. Adaptive SPH with Anisotropic Kernels

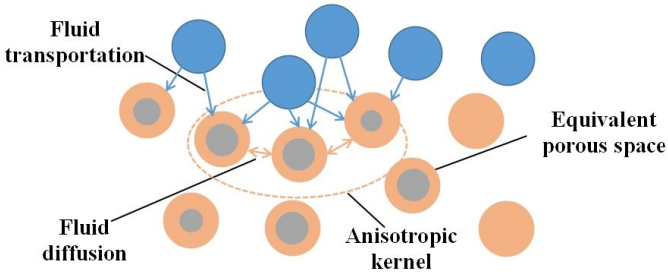

Figure 2: Equivalent continuous medium porous particle model for adaptive SPH. Pore-fracture in porous particle (orange) is modeled with continuous porosity (void space in orange particles) and permeability so that we could avoid complicated explicit modeling. The dotted ellipsoid denotes the anisotropic kernel of a solid particle, due to the distinctive layered structure, the permeability along the surface is bigger than that perpendicular to the surface. The arrow shows the fluid transportation between fluid particles (blue) and porous particles.

To reduce computation cost for anisotropy, here we detail the selective flexible and effective adaptive SPH, introduce the anisotropic kernel instead of isotropic kernel in traditional SPH. The kernel is characterized by different smoothing length along each axis. It can be expressed by a 3 by 3, second order smoothing tensor $\mathbf{G}$ which is real and symmetric. The corresponding anisotropic kernel function is

$$W(\mathbf{x}_{ij}, \mathbf{G}) = \frac{15}{\pi} \parallel \mathbf{G} \parallel (1 - \parallel \mathbf{G}\mathbf{x}_{ij} \parallel)^3, \tag{19}$$

where $\mathbf{G}$ rotates and stretches from the distance vector $\mathbf{x}_{ij}$ between two particles to $\mathbf{G}\mathbf{x}_{ij}$. The new kernel can find more neighbors along the earth, and can obtain more accurate weight distribution to enlarge the effect along the earth, while shrinking them in other directions. As shown in Fig.2, the adaptive SPH approximation to $\frac{\partial m_{pi}}{\partial t}$ for particle p_i is reformulated by searching the neighbor particles p_j:

$$\frac{\partial m_{pi}}{\partial t} = -\sum_j d_{ij}V_j(m_{pi} - m_{pj})\frac{\mathbf{G}\mathbf{x}_{ij} \cdot \nabla W(\mathbf{x}_{ij}, \mathbf{G})}{\|\mathbf{G}\mathbf{x}_{ij}\|^2 + 0.01/\|\mathbf{G}\|^2}, \tag{20}$$

here d_{ij} between two particles is:

$$d_{ij} = \mathbf{v}_{pj}\frac{\mathbf{r}_{ij}}{|\mathbf{r}_{ij}|}S_j^{\beta}, \tag{21}$$

where $\beta > 0$ is a user-defined parameter controling the diffusion.

Algorithm 1 PFEM-based Coupling Simulation.

Input: fluid particles, porous particles, PFEM mesh

for each *fluid and porous particle i* **do**
  find fluid and porous neighbors
  compute ρ_i and p_i
end for
for each *fluid particle* **do**
  add *viscosity force* and *surface tension force* from fluid neighbors
  add *pressure force* and *adhesion force* from porous neighbors
end for
for each *porous particle* **do**
  add *spring force* from porous neighbors
  add *pressure force* and *adhesion force* from fluid neighbors
end for
while *iteration* < *maxLoops or densityError* > *threshold* **do**
  for each *fluid particle* **do**
    predict $\mathbf{x}_i$ and $\mathbf{v}_i$
    compute predicted ρ_i and p_i
    compute corrective *pressure force*
  end for
  iteration++
end while
for each *fluid particle i* **do**
  update $\mathbf{v}_i$ and $\mathbf{x}_i$ with Euler integration
end for
for each *rigid body r* **do**
  calculate total $\mathbf{f}_r$ and τ_r from particles
  calculate $\mathbf{p}_r$ and $\mathbf{L}_r$ using $\mathbf{f}_r$ and τ_r
  update $\mathbf{x}_r$ and *rotation matrix* with *quaternion*
end for
for each *porous particle i* **do**
  synchronize $\mathbf{v}_i$ and $\mathbf{x}_i$ according to its parent *rigid body*
end for
for each *fluid and porous particle i* **do**
  calculate $\mathbf{v}_{pi}$ with Eq. 2
  evolute m_{pi} with Eq. 20
end for
for each *porous particle i* **do**
  if S_i, ϕ_i > *threshold* **then**
    convert *i* into fluid particle
  end if
end for
for each *fluid particle* **do**
  calculate diffusion with Eq.25
end for
couple fluid and structure with Algorithm 2
identify topology with surface modeling
if severe distortions *or* fracture *or* merging happens **then**
  generate new PFEM mesh
  update the rigid information for *porousparticles*
  update the link information for shape surface model
end if

4.3. Particle Finite Element Method

The Particle Finite Element Method (PFEM) [55, 56], a new generation of the particle method, which combines convective particle movement and a fixed mesh resolution, is designed for solving fluid-structure interaction problems, where moving fluid particles interact with the solid particles producing the deformation of the solid which in turn influences the fluid. In the PFEM approach, Lagrangian particles and meshing processes are alternated so that it inherits advantages of FEM structure that supports the differential equation solvers and Lagrangian formulation that allows to track the motion like the separation of each particle.

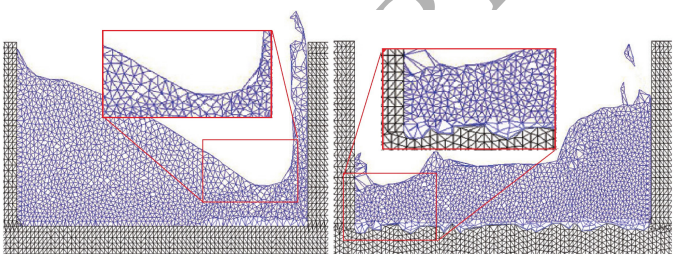

Figure 3: Extended Delaunay tesselation of fluid-solid coupling scene at two different times. The blue mesh denotes fluid areas while black mesh shows the deformable solid. Once the actual mesh deforms severely or the mesh is too obsolete for steps, new extended Delaunay mesh is regenerated.

In our method, porous domain is initialized with FEM mesh based on standard Delaunay discretization, then a typical step with the PFEM is summarized as the following steps: first solve coupled equations of motion including solid stress and strain; then move the mesh node to new position in terms of the time increment size; finally generate a new mesh based on extended Delaunay tesselation (EDT) [13] as shown Fig. 3 if the mesh regeneration process has not taken place for prescribed number of time steps or the Lagrangian motion is bringing severe distortions to the mesh. The criterion to join polyhedra is, if two Voronoi spheres have nearby centers (refer to Fig. 4), they must satisfy the following relationship:

$$|r_2 - r_1| \leq \|\mathbf{c}_1 - \mathbf{c}_2\| < \delta r_{rms}, \tag{22}$$

where r and $\mathbf{c}$ denote the radii and center of the spheres, δ is a non-dimensional constant, which is set to 0.1 in our expirment and r_{rms} is the root-mean-square radius. If two polyhedra belong to similar spheres, they will be joined together. The right figure in Fig. 4 shows a region with three different shape elements, triangle e_1, quadrilateral e_2, and pentagon e_3.

Fig. 5 shows the shape function definition for a polyhedral element consisting of m nodes $n_1, n_2, ..., n_m$. The shape function $N_i(x)$ corresponding to each node at internal position $\mathbf{x}$ is defined by the Voronoi Diagram to $\mathbf{x}$ in the element with the expression:

$$N_i(\mathbf{x}) = \frac{\frac{s_i(\mathbf{x})}{h_i(\mathbf{x})}}{\sum_{j=1}^{m} \frac{s_j(\mathbf{x})}{h_j(\mathbf{x})}}, \tag{23}$$

where $s_i(\mathbf{x})$ is the surface area of the corresponding Voronoi cell and $h_i(\mathbf{x})$ is the distance from $\mathbf{x}$ to n_i.

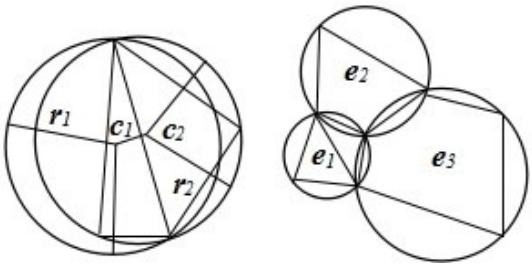

Figure 4: Left: Four nodes in near-degenerate position showing the empty circumcircles, which will be joined into one element in extended Delaunay tesselation. Right: Three polyhedral neighboring elements in extended Delaunay mesh.

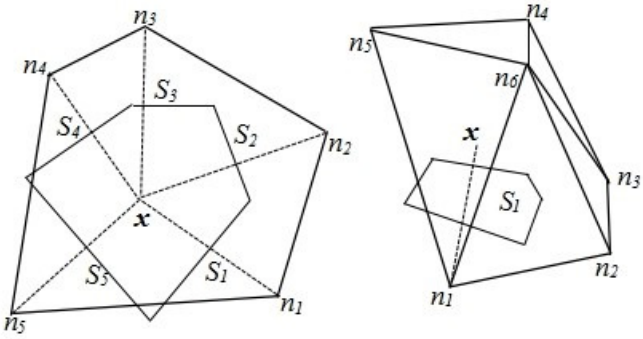

Figure 5: Shape function defined in 2D and 3D space.

In our experiments, as described in Algorithm 2, we adopt the variable-based fixation method, first fix W_k and solve ϕ, p with Eqs. 8 and 9, then fix ϕ, p and deal with Eq. 15 to compute W_k, finally correct the result iteratively until convergence. Then we calculate the fracture scheme based on results from pore stress analysis. The whole procedure in one cycle is detailed in Algorithm 2.

In the algorithm, the initial condition is the original pore pressure field, we set it according to the result of SPH pore pressure approximation. The greatest advantage of the MFEM, which is also shared with the FEM, is the easy imposition of the boundary conditions. The essential boundary conditions are introduced directly by assigning a value to the node parameters. The natural zero value condition is imposed automatically without any additional manipulation. In our experiments the boundary condition of pore flow field is a closed (impermeable) boundary, which means $\nabla \cdot (\frac{\mathbf{K}}{\phi\eta}(\nabla P^p - \nabla P^c - \rho\mathbf{g})) = 0$. And the boundary condition of stress field is a displacement boundary condition $\mathbf{u}_{boundary} = (0, 0, 0)$. The time step is based on the CFL condition for SPH

$$\Delta t \leq \lambda_v(\frac{h}{v_{max}}), \tag{24}$$

where $v_{max} = max\forall_t, \forall_i \|\mathbf{v}_i(t)\|$ is the maximum magnitude of the velocity throughout the simulation, and λ_v is a constant factor, being set to 0.4 in our experiments. In all the experiments performed, a maximum of 5 iterations in the iterative process are needed to reach a reasonable convergence.

Algorithm 2 Fracture Generation Scheme.

Input: PFEM mesh of porous media, fluid particles
Output: crack list *list* with certain number of points, normal $\mathbf{n}_p$ and area a_p

for each *node i* **do**
  calculate ϕ_i, p_i with Eqs. 8 and 12
end for
for each *node i* **do**
  calculate u_i with Eq. 15 in three directions
end for
go to 1 until convergence
for each *node i* **do**
  calculate σ_i, ε_i with Eq.16
  if $\lambda_{max}(\varepsilon_i) > threshold$ **then**
    add crack point *i* to *list*
    calculate U_i with Eq.18
    $\mathbf{n}_i$ = eigenvector for $\lambda_{max}(\varepsilon_i)$, $a_i = U_i/G$
  end if
end for
for i=0 to size of *list* **do**
  remove the corresponding links along the crack surface
end for
identify topology with shape modeling
update porous rigid information if needed
update porous particles if needed

5. Simulating Deformation and Fracture with unified Particles on Parallel Framework

After the deformation and fracture scheme is calculated in Section 4, we can now detail the geometric treatment based on the above unified framework.

5.1. Surface Modeling with Alpha Shape

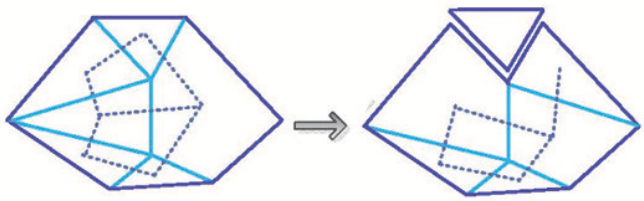

Figure 6: The link (dotted line) information to deal with fracture track. Links between elements are explicitly established during initialization, once the element shape changes, generate new links in separated elements and delete the inner links dynamically. When fracture happens, links along the track will be broken, linked particles is subdivided into two particles whose properties depend on the adjacent element volumes.

The geometric process during fracture is shown in Fig. 6, a link list is maintained to judge the topological change of porous

material. Every link is established between the inner surface of adjacent element, if a crack happens to break it, linked particles are subdivided to ensure the adjacent elements and their conserved volumes. Their velocity, saturation are set the same as parent particle, while the mass is distributed in accordance with the ratio of element volume.

To identify the external boundaries and simulate the merging of tiny fragments, an adaptive weighted alpha shape based method is proposed as shown in Fig. 7. The weight of point is proportional to its saturation and mass of particles. If two saturated fragments stick to each other, they tend to be caputerd as one component in alpha shape method, then we will establish new PFEM mesh and construct new links for the stick elements.

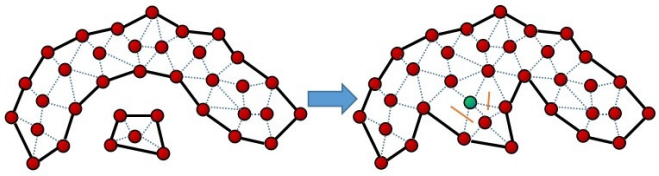

Figure 7: Weighted alpha shape and relink operation. The black line is the boundary calculated by alpha shape, blue dotted line denotes the PFEM mesh. When two fragments are near each other and the weight becomes large enough, they will merge to one component, here the green particle is surface particle before merging and becomes inner particle, after that, search the element containing green particle, two links (orange line) are constructed to maintain the new topological structure.

5.2. Saturation-sensitive Fluid Surface Reconstruction

As discussed in Section4.1, we adopt LLSPH [11] to simulate the self-diffusion in fluids based on the SPH model as

$$\rho \cdot \frac{\partial C_i}{\partial t} = \sum \frac{m_j}{\rho_j} \frac{4D_i D_j}{D_i + D_j} (C_i - C_j) \frac{\nabla W(\mathbf{r}_i - \mathbf{r}_j, h)}{\mathbf{r}_i - \mathbf{r}_j}. \quad (25)$$

Here D_i and D_j are the self-diffusion coefficients of particle i and j, C_i and C_j are the ratios of solute in fluids. Obviously, the concentration of fluid will diffuse from higher region to lower region. We calculate the saturation of MC mesh points with SPH interpolation, and take the average saturation as the saturation of corresponding triangle face. Then the color of triangle face is computed in HSL color space, where the lightness of color is linear to the saturation, ranging from 0.2 to 0.8 in our experiments with fixed hue and saturation in HSL.

5.3. Parallel Implementation

Our C++ code runs on PC with Intel Core i5-6200U CPU, 8G RAM memory and NVIDIA Geforce 940MX graphics card with CUDA 7.0. To initialize the tetrahedral mesh, we use the NETGEN (`sourceforge.net/projects/netgen-mesher`) and MeshLab (`meshlab.sourceforge.net`). Benefiting from our unified particle framework, most processes in our algorithm are feasible for parallel computation. The adaptive SPH based pore flow can be implemented in preview parallel SPH framework [57], then data is transfering back to CPU to the EDT modulus based on CGAL (`www.cgal.org`), finally coupling effects are computed in mulit-thread Eigen (`eigen.tuxfamily.org/dox`) solver and data is ready for the next cycle. All images are rendered offline by Pov-Ray (`www.pov-ray.org`) and VRay (`www.vray.com`).

6. Experimental Results

6.1. Simulation Results

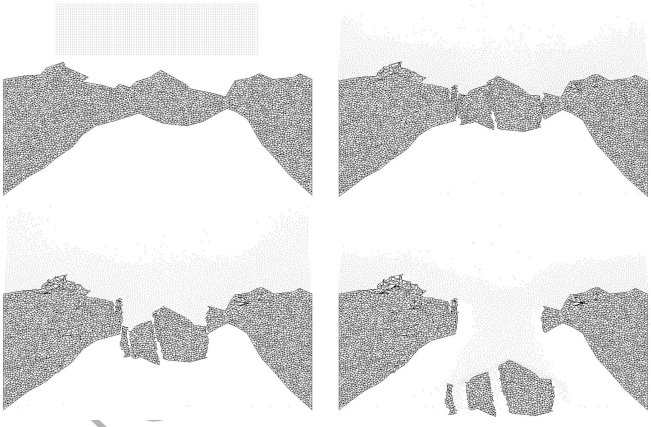

Figure 8: An example of porous structure collapsing in 2D. Fracture happens at the region with high pore pressure and saturation, which changes the mesh structure and gives rise to collapse. Tiny deformation and fragments are ignored in this example.

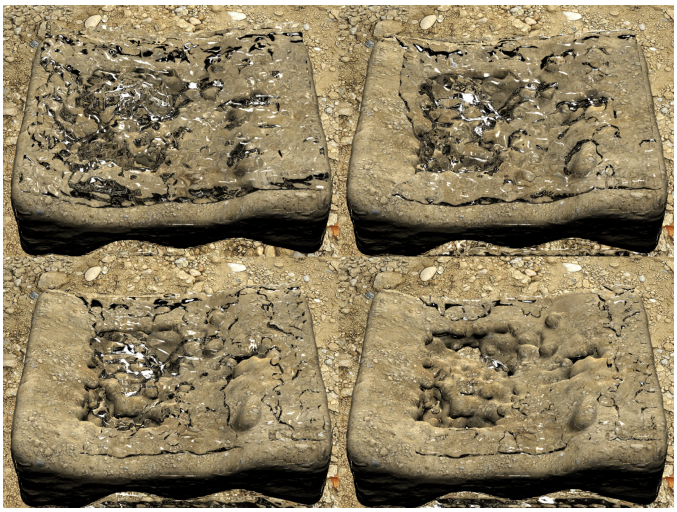

Figure 9: Porous structure collapsing in 3D scene. The bottom-right shot shows the final structure of porous media after fluid-structure coupling.

Based on the above method, we simulate fractures on different conditions in porous materials. All figures in this section are rendered in 1080×720 resolution with high-resolution fluid mesh.

To demonstrate a variety of porous structure (which is hard to visualize clearly in 3D scene), we simulate an example in 2D

space (shown in Fig. 8). The left and right boundary nodes are impermeable by setting porosity to zero in the example, meanwhile Fig. 9 shows the similar structure coupling in 3D space. Our new framework can simulate pore flow as well as the gradual deformation and fracture of porous media, which is usually ignored in preview works.

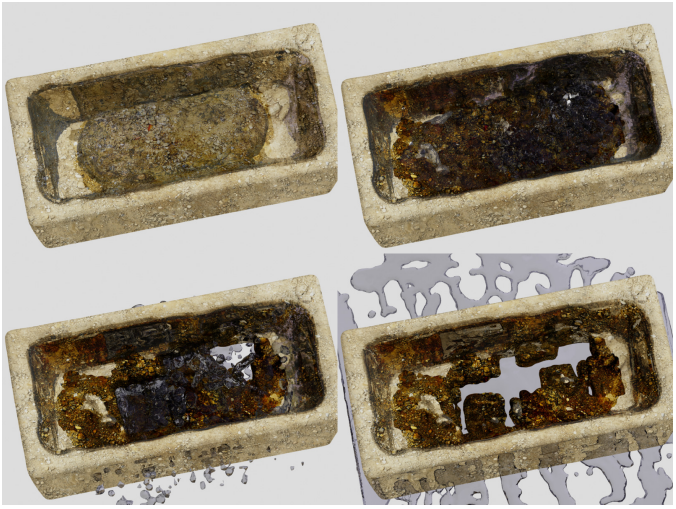

Figure 10: The scene of water deposition on porous cave. Water transports into porous media, bringing fracture expanded crack, finally breaks the solid structure of cave. The intensity of water is set inversely proportional to the concentration of slurry.

As Fig. 10 shows, when more and more fluid transports into porous cave in sink shape, great pore fluid pressure and stress start to bring fracture, destroying the whole structure of the porous cave, then the rest fluid washes the broken stone away. Anisotropy is also considered in permeability during fluid transportation and stress analysis in fracture generation. Inspired by physically relevant appearance models [58, 59], the gradual appearance of the porous media is adjusted by the color gradation of the texture mapping, such that wet material looks darker compared to dry material. But the gradual mapping will give rise to visual artifacts, while simple unified texture cannot show realistic results. It may be noted that, how to render wet porous media deserves much more additional work in terms of both rendering and appearance models, and they could not be fully justified in our current framework. Such efforts are necessary in our future work. In the interest of the main focus of our current approach, we simply apply the new rendering effects in Fig. 10 and Fig. 11. Obviously, our new particle method produces more support for complex fluid-rigid two-way coupling and fracture fragments shape including fluid transportation, diffusion, fluid-structure and fracture in a unified particle based framework, which avoids time-consuming mesh processing in FEM and complex coupling band in the previous hybrid method.

In Fig. 11, we modify the anisotropic permeability kernels in Fig. 10 to reduce the pore flow and pressure perpendicular to the surface. Finally no fracture happens, and only the cave surface takes some deformation, to show the result we remove the water in this scene. It is clear that adaptive SPH with anisotropic kernels can reflect the structure feature of porous material obviously and show controllable subsequent motion caused by pore flow phenomenon.

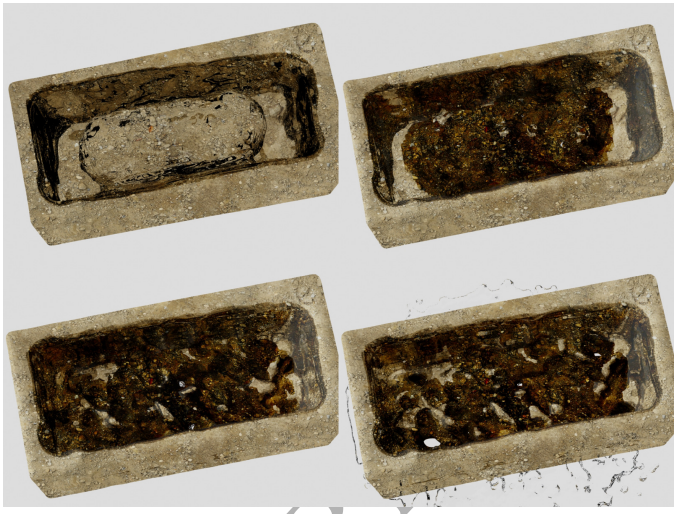

Figure 11: The same scene of water deposition with anisotropic kernel. The interaction including pore flow and pore pressure propagation perpendicular to the surface is reduced to 1/5. In this situation, little pressure results in no fracture but only deformation and small hole.

Figure 12: The water gushing-out caused by surface river's pore pressure. The first three figures are the shots from top view while the last figure is the close-up shot, water is removed for clear sight in this figure.

To demonstrate the water gushing-out during the process of earthwork for mine, which is usually caused by surface river or underground river. In Fig. 12 and Fig. 13, we set a 4 times higher permeability along the direction of surface relative to the vertical direction due to the layered structure of mine by changing the anisotropic tensor, so the pore flow propagated more along the surface than the vertical direction. Fig. 12 shows the situation of surface river, which is quite similar to Fig.10, we

Figure 13: The water gushing-out caused by underground river erosion. The figure shows the top view inside the mine road, which is eroded and teared by the pressure of underground river. The bottom-right figure is the profile from the top view.

add a few plain water to see clearly the solid structure. The porous cave breaks to several holes and drops fragments into the mine road. Meanwhile, Fig. 13 is the situation of underground river, where overmuch underground water is naturally producing high pressure in the initial steps, and it is set beneath the cave. Finally the high-pressure water erodes weak rock layers and destroys the mine road, and the gush of high pressure water flows into the mine road while its impact makes fracture segments flutter up and then drop or merge on the mine road. The bottom-right figure shows the mine road after destroying and merging with the profile from the top view. In the above two examples, boundary particles are set to be fully rigid.

Figure 14: A pavilion under continuous water erosion. Water is removed in the right figure to visualized the erosion clearly.

To demonstrate the efficiency of handling complex scenarios, Fig. 14 shows the scene of a complex pavilion model, containing a completely rigid bottom and columns with different anisotropic kernels to control the permeability in different directions ranging 1/2~2 times. Moreover, the columns are set with different modulus and porosity. The nearest two columns show higher permeability in y-axis, so that they have huge deformation compared with others. Finally, the fragments fell from the main body, merging on the corroded bottom as the right figure shows. And in Fig. 15 we employ our method in the complex modeling of 300, 000 elements (for mountain) and 320, 000 fluid particles to verify the robustness of our framework. In the scene, there is a tortuous tunnel inside the mountain, and flood rushes to the mountain, thus violent flow changes the structure of the tunnel. The red line in two sub-figures shows the new boundary of tunnel after simulation.

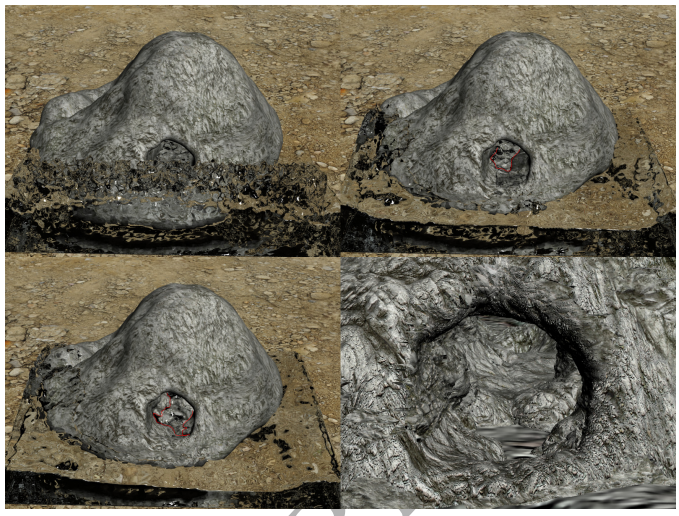

Figure 15: Coupling of flood and complex mountain model. 320k fluid particles and 300k elements are created during the simulation. The bottom-right close-up shot shows the deformed tunnel.

Table 2: Simulation statistics for the different scenarios.

Scenario	Solid Particles	Fluid Particles	Mesh Elements	Fragments
Collapsing	11610	4851	39914	12
Cave1	8052	801	26437	21
Cave2	8052	801	26059	6
Surface River	25629	3656	95251	23
Underground River	25629	8503	95251	25
Pavilion	26469	32928	97892	12
Mountain	70095	320702	309713	37

6.2. *Performance Evaluation*

The statistics for quantities in all the examples are documented in Table 2. It can be clearly seen that our model has advantages of fast pore flow calculation in anisotropic porous media, and the complex fluid-structure coupling. The number of particles is limited by the graphics memory in CUDA code. Table 3 documents the performance statistics, the frame-rate is the average number for animation sequences with no less than 600 frames, and this table also shows the average rendering time with VRay in the last column. Compared with other methods, our hybrid method shows efficiency on fluid-structure coupling. On the other hand, solving the partial differential equations is the main computational bottleneck though it has been accelerated in a multi-thread parallel fashion, further CUDA based

Table 3: Computation time statistics for the different scenarios. (In this table, EDT denotes the extended Delaunay tesselation, Average FPS denotes the average frame per second, and Average Render denotes the average time cost for rendering one frame with the third-party engine.)

Scenario	EDT (s)	Structure Coupling (s)	Fracture Process (s)	Average FPS	Average Render (s)
Collapsing	9.81	5.05	0.73	0.18	52.9
Cave1	5.97	2.15	0.37	0.40	40.5
Cave2	5.75	2.09	0.37	0.42	45.2
Surface River	13.20	19.82	1.16	0.04	92.6
Underground River	14.28	19.91	1.12	0.04	45.5
Pavilion	13.92	20.25	2.19	0.04	102.5
Mountain	30.72	109.26	5.65	0.01	95.6

Table 4: Comparison of recent works and our proposed method.

Recent Works	Model	Structure Coupling	Fracture or Tear	Render Results
Yang et al.[52]	Galerkin FEM	Yes	No	No
Lin[10]	SPH	No	No	Good
Um et al.[3]	Eulerian & PBD	No	Yes	Better
Our method	PFEM & ASPH	Yes	Yes	Better

GPU parallel acceleration is still in strong need.

Table 4 documents the comparison between our method and other methods for porous media animation. We have covered more aspects including fluid-structure coupling and fracture. The flexible PFEM also brings more detailed results with less computation cost compared with traditional mesh based methods.

6.3. Limitation

There are still some limitations in our approach that calls for further improvement in the near future. First, to simulate complex visual details, adaptive subdivision of particles is a natural method, while how to balance their physical and numerical correctness is challenging. Second, our deformation method still brings forth some less-desirable artifacts that should be overcome with better and more powerful physical models and computational strategies. Third, the fluid-structure coupling method is less ideal, leading to unstable situations during strong deformation in some of our experiments due to numerical features of certain models. Finally, the computational cost on mesh is the main bottleneck of our algorithm, a better acceleration strategy is necessary for more real-time applications.

7. Conclusion and Future Work

This paper has detailed a novel hybrid approach for fluid simulation penetrating through anisotropic porous substance, while considering fracture, dissolution, diffusion, etc. We proposed a new physical model based on the percolation theory to formulate the aforementioned phenomena and handle the dynamic properties and displacement field when pore flow occurs, and then, we employed a unified particle based numerical integration based on the anisotropic SPH approximation and PFEM mesh to solve the aforedocumented discrete model. Based on numerical discretization, we developed a stress analysis scheme to accomodate the rapid creation of cracks in high-pressure region. To further improve visual fidelity, we also dealt with slurry concentration driven dissolution coupled with slurry diffusion in fluid, and our hope is to ensure visual realism of slurry concentration details. Moreover, GPU platform in CUDA environment was adopted to accelerate our method's numerical performance. Through our extensive experiments in various scenarios, our method has exhibited effectiveness and usability in the complex, diverse media coupling.

At present, we choose to ignore many coupling effects in the interest of efficiency, such as evaporation, dry crack, and deposition, we shall continue our efforts to study geo-mechanics and involve other environmental factors (e.g., temperature, air), so that our framework can accomodate a more physically meaningful closed loop towards better, diverse visual effects. On the other hand, physically-sensitive appearance of the complex media needs much more additional work on illumination and appearance models to achieve better visual realism. In addition, a more effective acceleration strategy still requires our near-future investigation towards real-time graphics applications.

Appendix: Adaptive SPH with Anisotropic Kernel

In this paper, we choose adaptive SPH with anisotropic kernel as our particle solver, which is quite different from the traditional SPH. Now we briefly explicate the formulation derivation and kernel initialization for adaptive SPH.

In the SPH method, a field function can be numerically approximated as the summation over the nearest neighboring particles by using a smoothing function. One of the most widely used smoothing functions is the Spiky function. The Spiky smoothing function and its first derivative are documented as follows:

$$\begin{aligned} W(\mathbf{x},h) &= \alpha_d \cdot 10(1-D)^3 = \frac{15}{\pi h^6}(h-\|\mathbf{x}\|)^3, \\ \nabla W(\mathbf{x},h) &= \alpha_d \frac{1}{h}\frac{\mathbf{D}}{D}30(1-D)^2 = -\mathbf{x}\frac{45}{\pi h^6\|\mathbf{x}\|}(h-\|\mathbf{x}\|)^2. \end{aligned} \tag{26}$$

Here $\alpha_d = 3/2\pi h^3$ in three-dimensional space. $\mathbf{D}$ is the distance vector between two particles normalized by the scalar smoothing length h, $\mathbf{D} = \frac{\mathbf{x}}{h}$, where $\mathbf{x}$ is the real position vector between two particles.

Adaptive SPH with anisotropic kernel is proposed to respect features with the directional effects (more details can be found in [34]). The kernel is characterized by different smoothing length along each axis (please also see Fig. 16).

The kernel function in adaptive SPH can be written as a function of the tensor smoothing length $\mathbf{H}$ and the normalized position vector $\mathbf{D} = \mathbf{H}^{-1} \cdot \mathbf{x} = \mathbf{G} \cdot \mathbf{x}$. Tensor $\mathbf{G}$ has unit of the inverse of length. Therefore the corresponding anisotropic

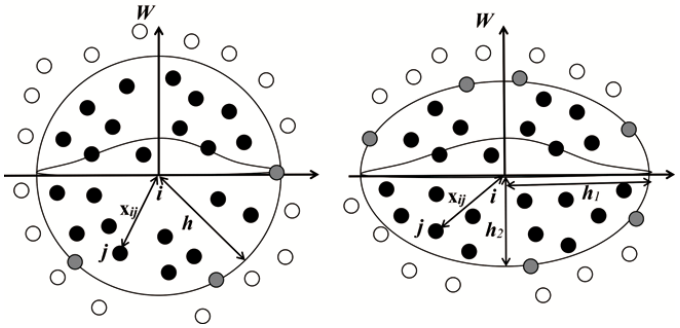

Figure 16: SPH (left) and adaptive SPH (right) approximations in 2D. Only particles within the influence domain of the smoothing function W for particle i can contribute in the summation process. In adaptive SPH, the influence domain of particle i is an ellipse rather than a circle in SPH.

kernel is

$$W(\mathbf{r},\mathbf{G}) = \frac{15}{\pi}\|\mathbf{G}\|(1-\|\mathbf{G}\mathbf{x}\|)^3,$$
$$\nabla W(\mathbf{r},\mathbf{G}) = -\frac{45}{\pi}\|\mathbf{G}\|\mathbf{G}^2\mathbf{x}\frac{(\mathbf{1}-\|\mathbf{G}\mathbf{x}\|)^2}{\|\mathbf{G}\mathbf{x}\|}. \quad (27)$$

The tensor $\mathbf{G}$ rotates and stretches the distance vector $\mathbf{x}$ to $\mathbf{G}\mathbf{x}$.

Consider the evolution of the absorbed fluid mass m_p in traditional SPH based on Eq. 4:

$$\frac{\partial m_{pi}}{\partial t} = \sum_j d_{ij}V_j m_{pj} \bigtriangledown^2 W(\mathbf{x}_{ij},h), \quad (28)$$

unfortunately, Eq. 28 does not obey the law of conservation of mass, let us consider two particles i and j as an example: the exchanged fluid mass calculated from particle i and particle j using Eq. 28 is not the same. So the heat conduction theory [11] on the SPH model is introduced and the formulation is recalculated as follows:

$$\frac{\partial m_{pi}}{\partial t} = -\sum_j d_{ij}V_j(m_{pi}-m_{pj})\frac{\bigtriangledown W(\mathbf{x}_{ij},h)}{\mathbf{x}}, \quad (29)$$

now it can be re-written as anisotropic formulation:

$$\frac{\partial m_{pi}}{\partial t} = -\sum_j d_{ij}V_j(m_{pi}-m_{pj})\frac{\mathbf{G}\mathbf{x}_{ij}\cdot\nabla W(\mathbf{x}_{ij},\mathbf{G})}{\|\mathbf{G}\mathbf{x}_{ij}\|^2+0.01/\|\mathbf{G}\|^2}, \quad (30)$$

where $0.01/\|\mathbf{G}\|^2$ is added to avoid too small $\mathbf{x}$.

To initialize tensor $\mathbf{G}$, we first decompose $\mathbf{G}$ with singular value decomposition (SVD):

$$\mathbf{G} = \mathbf{R}\mathbf{G_k}\mathbf{R^T}, \quad (31)$$

where $\mathbf{R}$ is a rotation matrix, with the column vectors corresponding to the axis direction, $\mathbf{G_k}$ is a diagonal matrix, with the diagonal element denoting the axis length. Given an appropriate assignment of $\mathbf{R}$ and $\mathbf{G_k}$, tensor $\mathbf{G}$ can be computed using Eq. 31 for simple geometric objects.

For complex geometric objects, however, the weighted principal component analysis (WPCA) is applied to analyze local anisotropy matrix [60]. WPCA begins by computing a weighted mean of data points to construct a weighted covariance matrix $\mathbf{C}$. The weighted mean $\mathbf{x}_i^w$ and the covariance matrix $\mathbf{C}_i$ of particle i are formulated as follows:

$$\mathbf{x}_i^w = \sum_j w_{ij}\mathbf{x}_j / \sum_j w_{ij},$$
$$\mathbf{C}_i = \sum_j w_{ij}(\mathbf{x}_j-\mathbf{x}_i^w)(\mathbf{x}_j-\mathbf{x}_i^w)^T / \sum_j w_{ij}. \quad (32)$$

Here, function w_{ij} is an weighting function with respect to particle i and j in the support radius $\|\mathbf{x}_i-\mathbf{x}_j\| < h_i$, and $w_{ij} = 1-(\|\mathbf{x}_i-\mathbf{x}_j\|/h_i)^3$.

With each particle, the SVD of $\mathbf{C}$ gives the directions of stretch/compression for deforming the smoothing kernel $\mathbf{W}$ in terms of eigenvectors and eigenvalues. The SVD yields $\mathbf{C} = \mathbf{R}\sum\mathbf{R}^T$, where $\mathbf{R}$ is a rotation matrix, and $\sum$ is a diagonal matrix with eigenvalues $\sigma_1 \geq ... \geq \sigma_d$. In order to prevent extreme deformations, $\sum$ is modified to enforce that the ratio between any two eigenvalues is smaller than user defined constant k_r (bigger than 1). Also, when the number of particles in the neighborhood is small, W is reset to a spherical shape $\mathbf{G} = k_n\mathbf{I}$. In our examples, we use $k_r = 4$, and $k_n = 0.5$. In addition, scaling factor $k_s = 1/\|\mathbf{C}\|$ enforces that $\|k_s\mathbf{C}\| \approx 1$, to keep the volume of W constant for particles with the full neighborhood, so

$$\widetilde{\sum} = \begin{cases} k_s diag(\sigma_1,\widetilde{\sigma_2},...,\widetilde{\sigma_d}) & N > N_\varepsilon \\ k_n\mathbf{I} & \text{otherwise} \end{cases}, \quad (33)$$

where $\widetilde{\sigma_k} = max(\sigma_k,\sigma_1/k_r)$, N is the number of neighboring particles and N_ε is a threshold constant. Then we produce $\mathbf{G}_i$ as a symmetric matrix of the form $\mathbf{G}_i = \frac{1}{h}\mathbf{R}\widetilde{\sum}\mathbf{R}^T$, where $1/h_i$ reflects the original radius of particle i.

Acknowledgements

This paper is partially supported by Natural Science Foundation of China under Grants 61532002 and 61672237, National Science Foundation of USA (IIS-0949467, IIS-1047715, IIS-1049448, and IIS-1715985), National High-tech R&D Program of China (863 Program) under Grant 2015AA016404, the Specialized Research Fund for Doctoral Program of Higher Education under Grant 20130076110008. The authors wish to thank the financial support from the program of China Scholarships Council No.201606140131. The authors also wish to thank all the anonymous reviewers for their insightful comments that have helped improve this paper's quality.

References

[1] F. Cappa, J. Rutqvist, Modeling of coupled deformation and permeability evolution during fault reactivation induced by deep underground injection of co 2, International Journal of Greenhouse Gas Control 5 (2) (2011) 336–346.

[2] N. Akinci, M. Ihmsen, G. Akinci, B. Solenthaler, M. Teschner, Versatile rigid-fluid coupling for incompressible sph, ACM Transactions on Graphics (TOG) 31 (4) (2012) 62.

[3] K. Um, T. Y. Kim, Y. Kwon, J. H. Han, Porous deformable shell simulation with surface water flow and saturation, Computer Animation & Virtual Worlds 24 (3-4) (2013) 247–254.

[4] M. Huber, B. Eberhardt, D. Weiskopf, Boundary handling at cloth–fluid contact, in: Computer Graphics Forum, Vol. 34, Wiley Online Library, 2015, pp. 14–25.

[5] G. Mitaritonna, A. Amorosi, F. Cotecchia, Experimental investigation of the evolution of elastic stiffness anisotropy in a clayey soil, Géotechnique 64 (6) (2014) 463–475.

[6] F. A. Dullien, Porous media: fluid transport and pore structure, Academic press, 2012.

[7] R. Narain, A. Samii, J. F. O'Brien, Adaptive anisotropic remeshing for cloth simulation, ACM transactions on graphics (TOG) 31 (6) (2012) 152.

[8] P. Li, X. Kong, D. Lu, Mathematical modeling of flow in saturated porous media on account of fluid-structure coupling effect, Journal of Hydrodynamics 4 (2003) 005.

[9] T. Lenaerts, B. Adams, P. Dutré, Porous flow in particle-based fluid simulations, ACM Transactions on Graphics 27 (3) (2008) 15–19.

[10] W. C. Lin, Boundary handling and porous flow for fluid-air interactions, Computers & Graphics 52 (C) (2015) 33–42.

[11] S. Liu, Q. Liu, Q. Peng, Realistic simulation of mixing fluids, Visual Computer 27 (3) (2011) 241–248.

[12] M. Liu, G. Liu, K. Lam, Adaptive smoothed particle hydrodynamics for high strain hydrodynamics with material strength, Shock Waves 15 (1) (2006) 21–29.

[13] S. R. Idelsohn, E. Onate, P. F. Del, The particle finite element method; a powerful tool to solve incompressible flows with free-surfaces and breaking waves, International Journal for Numerical Methods in Engineering 61 (7) (2004) 964–989.

[14] S. Idelsohn, E. Onate, F. Del Pin, A lagrangian meshless finite element method applied to fluid–structure interaction problems, Computers & Structures 81 (8) (2003) 655–671.

[15] H. Edelsbrunner, E. P. Mücke, Three-dimensional alpha shapes, ACM Transactions on Graphics (TOG) 13 (1) (1994) 43–72.

[16] W. E. Lorensen, H. E. Cline, Marching cubes: A high resolution 3d surface construction algorithm, in: ACM siggraph computer graphics, Vol. 21, ACM, 1987, pp. 163–169.

[17] M. Ller, D. Charypar, M. Gross, Particle-based fluid simulation for interactive applications, in: SCA '03: Proceedings of the 2003 ACM SIGGRAPH/Eurographics symposium on Computer animation, 2003, pp. 154–159.

[18] M. Ihmsen, J. Orthmann, B. Solenthaler, A. Kolb, M. Teschner, SPH Fluids in Computer Graphics, in: S. Lefebvre, M. Spagnuolo (Eds.), Eurographics 2014 - State of the Art Reports, The Eurographics Association, 2014. doi:10.2312/egst.20141034.

[19] K. Raveendran, C. Wojtan, G. Turk, Hybrid smoothed particle hydrodynamics, in: Eurographics/ACM SIGGRAPH Symposium on Computer Animation, SCA 2011, Vancouver, Bc, Canada, 2011, pp. 33–42.

[20] J. M. Hong, H. Y. Lee, J. C. Yoon, C. H. Kim, Bubbles alive., ACM Transactions on Graphics 27 (3) (2008) 15–19.

[21] F. Losasso, J. Talton, N. Kwatra, R. Fedkiw, Two-way coupled sph and particle level set fluid simulation., IEEE Transactions on Visualization and Computer Graphics 14 (4) (2008) 797–804.

[22] F. Sin, A. W. Bargteil, J. K. Hodgins, A point-based method for animating incompressible flow, in: ACM Siggraph/eurographics Symposium on Computer Animation, SCA 2009, New Orleans, Louisiana, Usa, August, 2009, pp. 247–255.

[23] N. Thürey, C. Wojtan, M. Gross, G. Turk, A multiscale approach to mesh-based surface tension flows, ACM Transactions on Graphics 29 (4) (2010) 1–10.

[24] T. Pfaff, N. Thuerey, M. Gross, Lagrangian vortex sheets for animating fluids, ACM Transactions on Graphics 31 (4) (2012) 13–15.

[25] C. B. Wang, Q. Zhang, F. L. Kong, H. Qin, Hybrid particle-grid fluid animation with enhanced details, The Visual Computer 29 (9) (2013) 937–947.

[26] N. Chentanez, M. Muller, T. Y. Kim, Coupling 3d eulerian, heightfield and particle methods for interactive simulation of large scale liquid phenomena., IEEE Transactions on Visualization and Computer Graphics 21 (10) (2015) 1116–28.

[27] K. Müller, D. A. Fedosov, G. Gompper, Smoothed dissipative particle dynamics with angular momentum conservation, Journal of Computational Physics 281 (2015) 301–315.

[28] S. R. Idelsohn, E. Onate, N. Calvo, F. D. Pin, Meshless finite element method, International Journal for Numerical Methods in Engineering 58 (6) (2003) 893–912.

[29] C. Jiang, C. Schroeder, A. Selle, J. Teran, A. Stomakhin, The affine particle-in-cell method, ACM Transactions on Graphics (TOG) 34 (4) (2015) 1–10.

[30] N. S. H. Chu, C. L. Tai, Moxi: real-time ink dispersion in absorbent paper, ACM Transactions on Graphics (TOG) 24 (3) (2005) 504–511.

[31] J. Kramer, J. Ravnik, R. Jecl, L. Škerget, Simulation of 3d flow in porous media by boundary element method, Engineering Analysis with Boundary Elements 35 (12) (2011) 1256–1264.

[32] M. L. Sawley, P. W. Cleary, J. Ha, Modelling of flow in porous media and resin transfer moulding using smoothed particle hydrodynamics, in: Second international conference on CFD in the minerals and process industries, 1999, pp. 473–478.

[33] G. Bicknell, R. Gingold, On tidal detonation of stars by massive black holes, The Astrophysical Journal 273 (1983) 749–760.

[34] J. M. Owen, J. V. Villumsen, P. R. Shapiro, H. Martel, Adaptive smoothed particle hydrodynamics: Methodology. ii., The Astrophysical Journal Supplement Series 116 (2) (1998) 155–209.

[35] N. Liu, F. Zhu, S. Li, G. Wang, Anisotropic kernels for meshless elastic solids, in: 12th International Conference on Computer-Aided Design and Computer Graphics (CAD/Graphics), IEEE, 2011, pp. 349–356.

[36] T. Lenaerts, P. Dutr, Mixing fluids and granular materials, Computer Graphics Forum 28 (2) (2009) 213C218.

[37] H. Darcy, Les Fontaines Publiques de Id Ville de Dijon, Dalmont, Paris, 1856.

[38] E. W. Washburn, The dynamics of capillary flow, Physical review 17 (3) (1921) 273.

[39] D. M. Anderson, Imbibition of a liquid droplet on a deformable porous substrate, Physics of Fluids 17 (8) (2005) 087104.

[40] R. Juanes, Nonequilibrium effects in models of three-phase flow in porous media, Advances in Water Resources 31 (4) (2008) 661–673.

[41] C. Kuijpers, H. Huinink, O. Adan, S. Erich, N. Tomozeiu, Transport of water–glycerol mixtures in porous materials studied with nmr imaging, WIT Transactions on Engineering Sciences 89 (2015) 513–525.

[42] M. J. Blunt, Flow in porous mediapore-network models and multiphase flow, Current opinion in colloid & interface science 6 (3) (2001) 197–207.

[43] D. Nikanśhin, A. Nikiforov, Modeling of transfer of particles of different size by a two-phase filtration flow, Journal of engineering physics and thermophysics 73 (3) (2000) 481–485.

[44] Z.-j. Luo, J.-b. Liu, L. Li, Three-dimensional full coupling numerical simulation of groundwater dewatering and land-subsidence in quaternary loose sediments, CHINESE JOURNAL OF GEOTECHNICAL ENGINEERING-CHINESE EDITION- 30 (2) (2008) 193.

[45] P. C. Lichtner, Q. Kang, Upscaling pore-scale reactive transport equations using a multiscale continuum formulation, Water Resources Research 43 (12).

[46] T. Keller, D. A. May, B. J. Kaus, Numerical modelling of magma dynamics coupled to tectonic deformation of lithosphere and crust, Geophysical Journal International 195 (3) (2013) 1406–1442.

[47] B. Malvoisin, Y. Y. Podladchikov, J. C. Vrijmoed, Coupling changes in densities and porosity to fluid pressure variations in reactive porous fluid flow: Local thermodynamic equilibrium, Geochemistry, Geophysics, Geosystems 16 (12) (2015) 4362–4387.

[48] N. Chentanez, T. G. Goktekin, B. E. Feldman, J. F. O'Brien, Simultaneous coupling of fluids and deformable bodies, in: Proceedings of the 2006 ACM SIGGRAPH/Eurographics symposium on Computer animation, Eurographics Association, 2006, pp. 83–89.

[49] A. Robinson-Mosher, T. Shinar, J. Gretarsson, J. Su, R. Fedkiw, Two-way coupling of fluids to rigid and deformable solids and shells, in: ACM Transactions on Graphics (TOG), Vol. 27, ACM, 2008, p. 46.

[50] R. Hilfer, Macroscopic capillarity and hysteresis for flow in porous media., Physical Review E 73 (1 Pt 2) (2006) 302–309.

[51] M. Becker, M. Teschner, Weakly compressible sph for free surface flows., in: ACM Siggraph/eurographics Symposium on Computer Animation, SCA 2007, San Diego, California, Usa, August, 2007, pp. 209–217.

[52] Y. Yang, X. F. Song, F. D. Zheng, L. C. Liu, X. J. Qiao, Simulation of fully coupled finite element analysis of nonlinear hydraulic properties in land subsidence due to groundwater pumping, Environmental Earth Sciences 73 (8) (2015) 4191–4199.

[53] D. Gross, T. Seelig, Fracture mechanics: with an introduction to micromechanics, Springer Science & Business Media, 2011.

[54] B. Ganis, V. Girault, M. Mear, G. Singh, M. F. Wheeler, Modeling fractures in a poro-elastic medium, Oil & Gas Science & Technology C Revue Difp Energies Nouvelles 69 (4) (2014) 515–528.

[55] E. Nate, S. R. Idelsohn, F. Del, R. Aubry, The particle finite element method. an overview, International Journal of Computational Methods 1 (2) (2004) 267–307.

[56] E. Onate, A. Franci, J. M. Carbonell, A particle finite element method for analysis of industrial forming processes, Computational Mechanics 54 (54) (2014) 85–107.

[57] T. Harada, S. Koshizuka, Y. Kawaguchi, Smoothed particle hydrodynamics on gpus, in: Computer Graphics International, SBC Petropolis, 2007, pp. 63–70.

[58] J. Dorsey, H. Rushmeier, Advanced material appearance modeling, in: ACM SIGGRAPH 2009 Courses, ACM, 2009, p. 3.

[59] H. Wu, J. Dorsey, H. Rushmeier, Inverse bi-scale material design, ACM Transactions on Graphics (TOG) 32 (6) (2013) 163.

[60] J. Yu, G. Turk, Reconstructing surfaces of particle-based fluids using anisotropic kernels, ACM Transactions on Graphics (TOG) 32 (1) (2013) 5:1–5:12.